

Oblique incidence deposition of Cu/Cu(001): Enhanced roughness and ripple formation

Frits L. W. Rabbering, Georgiana Stoian, Raoul van Gastel, Herbert Wormeester,* and Bene Poelsema
 MESA+ Institute for Nanotechnology, University of Twente, P.O. Box 217, 7500 AE Enschede, The Netherlands
 (Received 5 January 2010; revised manuscript received 19 February 2010; published 15 March 2010)

Polar angle of incidence, substrate temperature, and atom flux are of key importance to the self-organization process on a substrate surface during oblique incidence deposition. The substantial influence of these parameters in homoepitaxial growth on Cu(001) is studied using scanning tunneling microscopy, high-resolution low-energy electron diffraction, and extensive growth simulation. The quantitative simulations reproduce the experimentally observed phenomena in great detail provided the steering effect is incorporated and accurate barriers for interlayer transport are used. Both experimental techniques reveal the formation of rectangular mounds for sufficiently large angles of incidence that are initially elongated in the direction perpendicular to the deposition plane of incidence. The simulations show a transition from perpendicular to parallel orientation, which occurs through pyramid formation at a coverage that depends on the angle of incidence and the substrate temperature. The elongation of the islands can be quite strong, leading to ripple formation and a very strong roughening of the growth front. The enhanced roughening of the growth front, compared to the already rough growth observed at normal incidence, is identified as super Poisson growth.

DOI: [10.1103/PhysRevB.81.115425](https://doi.org/10.1103/PhysRevB.81.115425)

PACS number(s): 68.55.A-, 81.15.Aa, 68.49.Jk, 68.35.Fx

I. INTRODUCTION

Precise tailoring of the morphology of epitaxial films with a thickness greater than a few monolayers (ML) is a complicated task that requires a thorough understanding of all the atomic mechanisms that are relevant. Each of these may influence the structures that form during growth in a different way. The final morphology can be controlled with only a few macroscopic parameters: temperature, growth rate, and the angle of incidence of the deposition beam. The polar angle of incidence is of particular interest, because it allows to grow anisotropic structures like those found in columnar growth. The orientation of these epitaxial columns depends on the angle of incidence of the deposition beam, an observation that is described phenomenologically by the so-called tangent rule.¹ Since this observation, the angle of incidence has matured to a tool to induce anisotropic material properties such as magnetic anisotropy² and designed optical^{3,4} behavior. Magnetic films are particularly well suited to study the influence of deposition angle, because their magnetic behavior is extremely sensitive to anisotropy of the grown structures. Co-Ni films grown on silicate develop a columnar structure for an angle of incidence greater than 60° with respect to the surface normal.⁵ Films with a thickness below 30 nm show a very different magnetic behavior compared to thicker films. In the thicker films, a hard magnetic axis forms parallel to the column orientation, while for thinner films the magnetic hard axis is parallel to the interface and perpendicular to the plane of the deposition beam.⁶ A similar perpendicular orientation of the magnetization with respect to the plane of incidence occurs for ultrathin Co films deposited at grazing incidence on Cu(001).⁷⁻¹⁰ However, while the morphology observed after oblique incidence deposition is generally and qualitatively explained with geometric shadowing of the incoming flux, this concept fails to explain on an atomic scale the observed anisotropy for the ultrathin and especially the submonolayer thick films. Instead, it is explained by an effect coined as steering:⁷ protrusions on the

surface act as attractors for incoming material. The trajectories of incoming atoms are altered by dipolar interactions between incident atoms and protrusions in the substrate morphology. This effect is paramount in understanding the initial phases of oblique incidence growth that is more often than not determining the final morphology of a thin film. Homoepitaxial growth provides an excellent framework to study the steering effect⁷⁻¹⁰ as a function of angle of incidence, because it avoids complications due to intermixing and lattice mismatch present and important in heteroepitaxy. In this paper we report a combined, quantitative experimental and simulation study of the influence of the angle of deposition, and substrate temperature on the morphology in Cu(001) homoepitaxy.

II. STEERING

The influence of the steering effect on growth was first suggested by Shevchik¹¹ and later found experimentally in high-resolution low-energy electron diffraction (HR-LEED) measurements of grazing incidence homoepitaxial growth on Cu(001).^{7,8,12} Already during submonolayer deposition, a slight elongation of the adatom islands, perpendicular to the plane of incidence, is observed and the steering effect can be viewed as an anisotropic uphill diffusion current effect. Deposition of approximately 10 ML of Cu leads to the formation of elongated structures that are quite well ordered along the plane of incidence. After 40 ML deposition a ripple structure with pronounced facet angles forms. These results demonstrate that the facets of the illuminated side, the shadow side, and the two side walls develop in a quite well defined but very different manner. The growth of these structures was recently described theoretically by Shim and Amar.¹³ They report the development of ripple structures and a change in orientation of these ripples for very rough, thick films deposited at grazing incidence. Unfortunately, their calculations were done with a barrier for interlayer mass transport that is much higher than what was recently determined

for the Cu(001) surface.¹⁴ This leads to a rough growth front from the very start, while experimentally a more layer-by-layer-like growth is observed at temperatures of 250 K and higher.^{12,14-17}

To study the morphology evolution for oblique incidence deposition on Cu(001), we use a simulation program which uses diffusion barriers that are capable to quantitatively describe the growth at normal incidence in a suitable temperature window.¹⁴ The observed anisotropy in the submonolayer range for grazing incidence deposition has been used to determine the attractive dipolar interaction between the incident atoms and the substrate.^{18,19} These ingredients provide a simulation scheme that can be used to study the influence of oblique incidence deposition on the surface morphology. In the following, we will first present the simulated morphology after 40 ML deposition as a function of angle of incidence and temperature and compare these with scanning tunneling microscope (STM) measurements. Existing high-resolution low-energy electron diffraction measurements^{7,8,12,20} are complemented with more extensive measurements of the facets that form during growth. The results from experiments and simulations exhibit a high degree of correspondence, providing a firm reason why the simulations we present can be used with confidence to investigate the processes involved in the development of the elongated structures. The detailed analysis we present includes: (1) the rotation of the elongation direction upon increase in the thickness. The coverage at which this takes place depends on the angle of incidence of the deposition and the substrate temperature. (2) The strong roughening of the growth front during oblique incidence deposition that leads to the observation of super Poisson roughening, i.e., the interface roughening is stronger than that resulting from a simple hit-and-stick deposition process with a homogeneous flux of atoms. (3) The evolution of the average mound shape which holds a surprisingly large amount of material in the higher layers of the mounds.

III. EXPERIMENTAL AND SIMULATION DETAILS

The experiments were performed in two different UHV systems, one equipped with HR-LEED and the other with a homebuilt STM. The base pressure was $<1 \times 10^{-10}$ mbar and $<2 \times 10^{-10}$ mbar, respectively. The precision aligned Cu(001) crystals²¹ were cleaned by sputtering using 800 eV Ar⁺ ions and annealing at a temperature of 750 K. The impurity level is kept below the Auger electron spectroscopy detection limit. Further inspection was performed with HR-LEED, which ultimately showed an average terrace length in excess of 100 nm,^{7,12,20,22} and with STM. A thoroughly desulfurized thermal evaporation Cu source was used in both systems for grazing incidence deposition (polar angle typically 80°) along the [110] azimuth. In the UHV system equipped with the HR-LEED, the evaporation rate was repeatedly verified for normal incidence growth with *in situ* thermal energy atom scattering.^{14,18,22-26} A deposition rate of 0.5 ML/min at grazing incidence was used in this case. The calibration of the deposition rate was inferred in the STM UHV system from images taken after submonolayer deposition at a polar angle of 80° and at a substrate temperature of

250 K. This provided a rate of 0.6 ML/min. After deposition, the samples were quenched to a temperature below 120 K to avoid coarsening effects during the analysis of the surface morphology.

Oblique incidence deposition was simulated with a kinetic Monte Carlo (kMC) scheme on a lattice of 512×512 atoms, as described in detail elsewhere.^{14,18,19} Activation barriers for intralayer processes, as determined by Biham *et al.*,²⁷ were used. Two interlayer diffusion processes were incorporated simulating transport via $\langle 110 \rangle$ - and $\langle 100 \rangle$ -oriented step segments. An Ehrlich-Schwoebel barrier of 120 meV and -5 meV, respectively, was used for these processes.¹⁴ Kink sites that are frequently present in the energetically favored $\langle 110 \rangle$ step are treated as $\langle 100 \rangle$ microfacets. To prevent overhangs, an immediate downfunneling process is incorporated.²⁸ This simulation scheme provides a surface morphology for normal incidence deposition that has average properties like interface roughness and distance between mounds similar to experimental observations for multilayer growth over a temperature range between 230 and 290 K.^{14,18} This was only possible by tuning the fast-diffusion processes.²⁷ Without this, the fast majority of the simulation time would be spent on fast processes that do not alter surface morphology like diffusion along steps. The end result of diffusion along steps is that the diffusing atom will eventually be more strongly bound in one or more possible final positions. This diffusion process is so fast that it does not influence any of the other processes, but does require a major part of the CPU time. It can thus be slowed down without consequences for the growth morphology as long as the probability of the various final positions is not altered. Following the suggestion of Biham *et al.*,²⁷ we incorporated an artificial suppression of paths with an energy barrier below 400 meV.^{14,18}

The calculated impact position of an atom in a deposition event was obtained from a trajectory calculation. The initial velocity of these atoms followed a Maxwell Boltzmann distribution in order to comply with the velocity distribution of the experimentally used deposition source. Every incoming atom experiences a potential that mimics both the short-range electron overlap effects, as well as the long-range dipole-dipole interaction. The parameters have been taken from previous results.^{18,19} The atom-substrate potential depends on the actual morphology. Both the experiments and the simulations show an extensive formation of $\{111\}$ facets. The activation energy for diffusion on a $\{111\}$ surface is very low compared to a $\{100\}$ surface.²⁹ The movement of an adatom on a $\{111\}$ facet is therefore treated as an instantaneous move down the facet, where the atom is incorporated in the advancing step edge on this facet. This treatment corresponds to assuming step propagation on the relatively small facets.

IV. MORPHOLOGY AFTER 40 ML OF OBLIQUE INCIDENCE DEPOSITION

A. Simulation results

Electron-diffraction measurements have demonstrated the influence of the deposition angle and deposition temperature

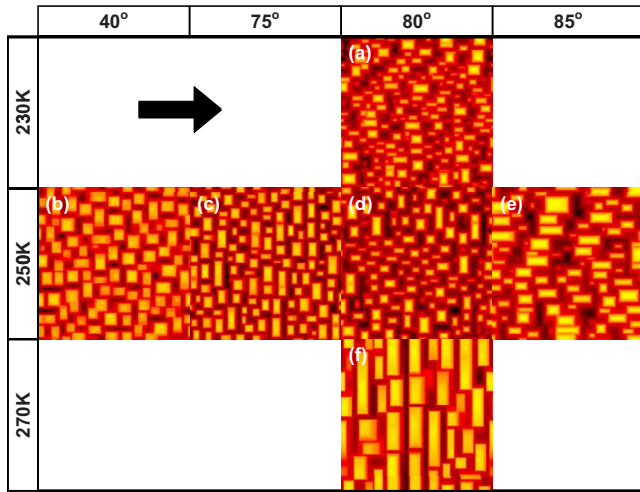


FIG. 1. (Color online) Simulated topographic images of the surface morphology after growing 40 ML at a rate R of 1 ML/min at different deposition angles (horizontal) and temperatures (vertical). The temperatures are (a) 230 K, [(b)–(e)] 250 K, and (f) 270 K. The polar deposition angles are (b) 40°, (c) 75°, [(a), (d), and (f)] 80°, and (e) 85°. Each window is 130 nm (512 atoms) wide. The arrow denotes the deposition direction.

on the surface morphology in Cu homoepitaxy.^{8,20} Near normal incidence deposition results in a fourfold symmetric morphology, while at grazing incidence the formation of a ripple structure is reported. The formation of ripples, observed after deposition of 40 ML, is found only in a limited temperature window. The ripples are present at 250 K, but absent at 200 and 300 K. To understand this ripple formation, we studied in our simulation scheme the influence of angle of incidence of the deposition beam and surface temperature. Figure 1 depicts the simulated surface morphology after deposition of 40 ML for various angles of incidence and substrate temperatures.

A deposition rate of 1 ML/min was used in all simulations. This is similar to the experimental rates. The depicted simulated morphologies show that mound formation takes place at a polar angle of 40° and 250 K. The mounds are ordered in a checkerboardlike pattern, shown in Fig. 1(b). This is very similar to experimental observations of normal incidence growth.^{14,22} For oblique deposition, the main difference is that during growth the center of mass of the mounds moves in the direction of the deposition source. Around 80° polar angle of incidence, a dramatic change in mound formation occurs. Below this angle, the formation of rectangular mounds perpendicular to the deposition plane is observed [Fig. 1(c)], while at a very grazing incidence angle of 85° [Fig. 1(e)], the mound orientation is parallel to the plane of incidence. Similar elongated mounds parallel to the deposition plane are also observed for a polar angle of incidence of 80° at 230 K [Fig. 1(a)]. This rotation was reported previously by Shim and Amar¹³ for their simulations of grazing incidence deposition. At a more elevated temperature of 270 K very well-defined ripples develop perpendicular to the plane of incidence. Our results demonstrate that the actual morphology is very sensitive to temperature and deposition angle. A simulation under the experimental conditions used

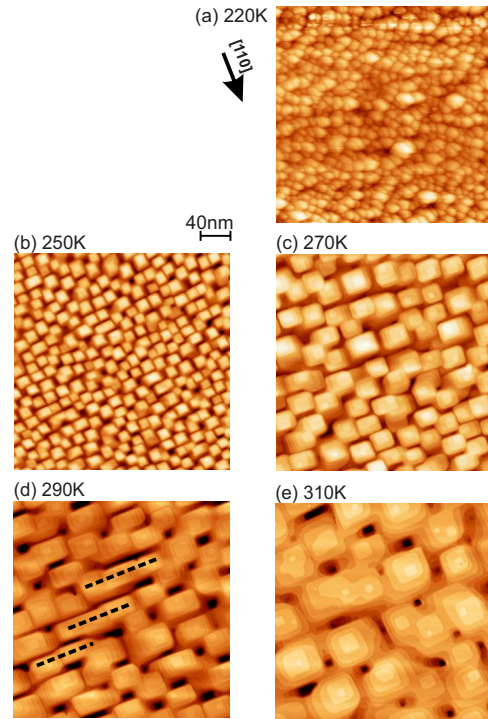


FIG. 2. (Color online) STM topographs after growth of 40 ML Cu/Cu(001) at a polar angle of incidence of 80° with a deposition rate of 0.6 ML/min and at various substrate temperatures, ranging from 220 to 310 K. The black arrow indicates the deposition direction that corresponds to the [110] azimuth. The image size is 290 × 290 nm², obtained with a tunneling current 0.4 nA and tunneling voltage 0.4 V. The dashed lines in the topograph at 290 K indicate the alignment of mounds.

extensively by van Dijken *et al.*,^{8,20} i.e., a substrate temperature of 250 K and a polar angle of incidence of 80°, shows anisotropic mounds that are oriented either along or perpendicular to the deposition beam. The simulations suggest under these conditions 40 ML deposition results in a transition between two rotational regimes [Fig. 1(d)]. Our simulations also suggest that the preparation of a well-defined ripple structure requires a slightly higher temperature of 270 K. At temperatures lower than 250 K a rotation of the elongated mounds occurs before the mounds can merge into a ripple-like structure. The size of the ripples obtained in the simulation at 270 K indicates that simulations at higher temperatures will be strongly affected by the size of the simulation grid. Present capabilities unfortunately limit the simulations to a grid size of 512 × 512 atoms.

B. Temperature-dependent STM measurements

Figure 2 displays representative STM topographies acquired after deposition of 40 ML of Cu on Cu(001) at a polar angle of 80° in the temperature window from 220 to 310 K.

The black arrow in the upper corner of Fig. 2(a) indicates the direction of deposition. It is identical for all experiments and corresponds to the [110] azimuth. For all temperatures, the edges of the mounds are orientated along the energetically favorable $\langle 110 \rangle$ directions of the Cu(001) surface. The

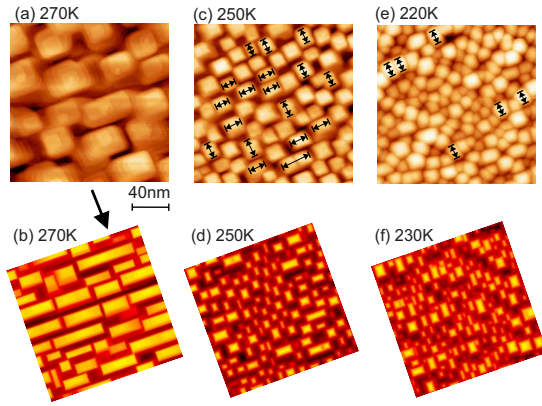


FIG. 3. (Color online) Comparison of surface morphologies inferred from experiments (upper row) and simulations (lower row) after the growth of 40 ML Cu/Cu(001) at a polar angle of 80° for different surface temperatures. The plane of incidence of the incoming atomic beam is indicated by the black arrow in between pictures and corresponds to the [110] azimuthal direction. Image sizes are $145 \times 145 \text{ nm}^2$ for STM topographies and $130 \times 130 \text{ nm}^2$ for simulated morphologies.

distance between the mounds and the size of the features increase with substrate temperature, as is also observed for normal incidence deposition.^{14,22} The STM images clearly show the formation of elongated mounds perpendicular to the deposition direction for temperatures from 270 to 290 K. The shape anisotropy of the mounds is not the only difference compared to normal incidence deposition. The mounds are no longer arranged in a checkerboardlike pattern. Instead, a strong preference for alignment in rows is found for the elongated shape. This effect is strongest after deposition at 290 K (indicated by the dashed lines), but is also present at 250 and 310 K. This alignment is a clear indication of ripple formation, which is evident in our simulations at 270 K. The anisotropy of the mounds increases with surface temperature up to 290 K. At 310 K, the asymmetry breaks down due to the enhanced surface mobility and the morphology almost turns into a checkerboardlike pattern, similar to what is obtained for normal incidence deposition. The investigation of the surface morphology after deposition at the low temperature of 220 K is quite problematic, Fig. 2(a) illustrates this. The small feature size and the relatively broad apex radius of the STM tip result in strong convolution effects. This prevents the recording of images over large areas with sufficient resolution.

A direct comparison of the STM images and the morphology obtained from kinetic Monte Carlo simulations is shown in Fig. 3. The simulation results have been rotated in order to align the deposition direction, indicated by the black arrows. At 270 K, both morphologies [Figs. 3(a) and 3(b)] exhibit elongated mounds with the same orientation. The simulations show a more profound ripple formation compared to the experimental results. This ripple formation is the result of interlayer mass transport perpendicular to the deposition direction, which favors the coalescence of mounds in this direction. The simulations may overestimate this effect. The simulations also show that the ripples are separated by deep trenches. The STM measurements also show larger height

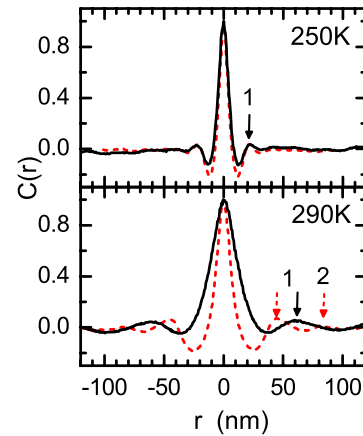


FIG. 4. (Color online) Line profiles of the averaged autocorrelation images calculated from STM images obtained at the indicated temperature (Fig. 2). Profiles perpendicular (solid black line) and parallel (dashed red line) to the deposition direction are shown in black and red, respectively.

variations along the plane of incidence compared to those along the normal of this plane. At 230 K, the simulated topography of Fig. 3(f) exhibits elongated structures parallel to the deposition direction, i.e., with an orientation 90° rotated with respect to the mounds obtained at 270 K in Fig. 3(b). Although the poor quality of the images of films deposited at 220 K hampers their interpretation, a few mounds, highlighted by double sided arrows in Fig. 3(e), show a clear elongation parallel to the deposition direction. For the intermediate deposition temperature of 250 K, mounds with mixed orientations (parallel or perpendicular to the beam) are obtained both in the simulated and in the experimental morphology. For the experimental case the orientation of the mounds is indicated by double sided arrows pointing in the direction parallel or perpendicular to the plane of incidence. The STM measurements are thus consistent with the general observations from the simulations, i.e., a change in orientation of the elongation direction of the mounds. The ripple formation is overestimated in the simulations. Finite angular spread of the incident beam may be held responsible for these slight differences.

C. Shape anisotropy deduced from STM

A more quantitative description of the experimentally observed average surface morphology is obtained from the autocorrelation image $C(r)$ of the STM topographs. This allows to display the average properties of typically seven STM images taken at different locations on the surface after a deposition experiment. Figure 4 shows characteristic line profiles parallel and perpendicular to the deposition plane of the autocorrelation image. The full width at half maximum of the main peak represents the average size s of the mounds. For all temperatures we observe that s is broader in the direction perpendicular to the deposition plane. This indicates an elongation of the mounds in this direction. The average aspect ratio (AR) or shape anisotropy of the structures $AR = s_{\perp}/s_{\parallel}$, is shown in Fig. 5. The shape anisotropy increases

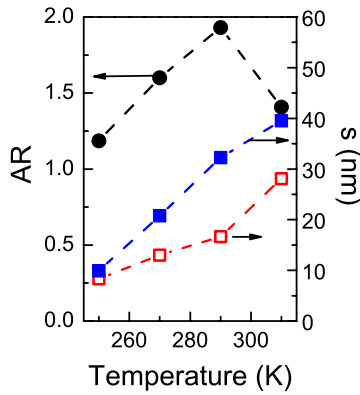


FIG. 5. (Color online) Measured average mound size (blue solid square s_{\perp} , red open square s_{\parallel}) and average AR for the temperature-dependent STM measurements shown in Fig. 2 as derived from averaged autocorrelation line profiles as depicted in Fig. 4.

from 250 to 290 K up to a value of around 2 followed by a decrease to a value of 1.4 for growth at 310 K. The simulations at 250 K after 40 ML deposition show an $AR \approx 1$ for 250 K, while the ripple pattern simulated for 270 K results in an aspect ratio of 5, much higher than observed experimentally. The STM images at 220 K show a too large height variation in relation to the lateral feature size to provide an useful autocorrelation image.

The position of the first-order maximum in the $C(r)$ line profiles represents the average distance L between mounds. The distance in the direction parallel and perpendicular to the plane of incidence is quite similar after deposition at 250 K, but increases to larger distances with temperature. Also for the measurement at 290 K, the distance in the direction perpendicular to the deposition plane of incidence (solid black arrow labeled 1 in Fig. 4) is larger than that for the direction parallel (dashed red arrow labeled 1) to the deposition plane of incidence. At 270 K (not shown) and 290 K, even a second-order maximum can be discerned along the incidence direction (dashed red arrow labeled 2). This indicates an enhanced ordering in this direction.

D. Facet slopes deduced from HR-LEED

The experimental diffraction pattern obtained after deposition of 40 ML at grazing incidence (80°) is dominated by features related to various slopes of the facets on the different sides of the mounds present on the surface.^{7,8} Figure 6(a) shows a typical experimental diffraction pattern obtained after deposition of about 40 ML at a polar angle of 80° at a temperature of 250 K.

A simulated diffraction pattern of this situation is displayed in Fig. 6(b). This and other simulated diffraction images were calculated in the kinematic approximation with diffraction conditions similar to experimental conditions. The experimental and simulated diffraction images in Fig. 6 exhibit similar features. Both images show a mirror symmetry with respect to the plane of incidence of the atomic copper beam. The position of the diffraction features associated with the facet angles present on the surface is also quite similar. The relative intensity of these features differs, which is ex-

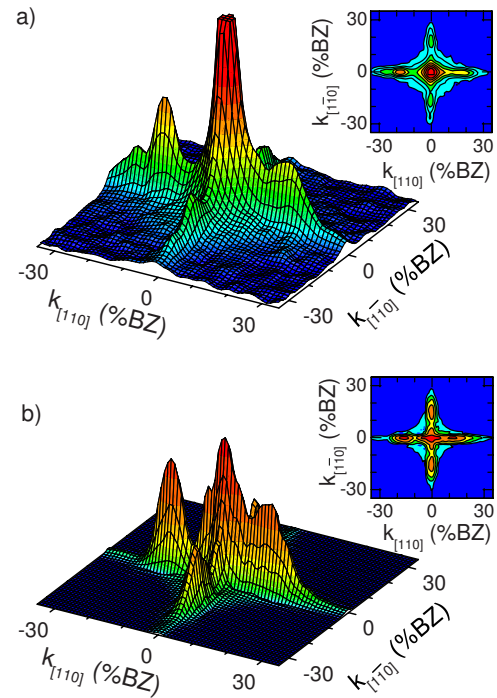


FIG. 6. (Color online) Diffraction profiles after depositing 36.5 ML at 80° at $T=250$ K. (a) The experimental diffraction image and (b) the corresponding simulation result. The phase is $S_z=3.9$ (176 eV). The plane of incidence for the copper atom beam is along the $[110]$ direction.

pected since we neglect dynamic effects in the calculation of the simulated diffraction pattern. Also a nonideal quench and flux variations in the experiment across the incident-beam spot may contribute to the observed differences.

The facet slopes of the different sides of the mounds could be evaluated from the relation between the perpendicular and parallel phase of facet related diffraction features. This is revealed in an intensity scan of the perpendicular phase versus $k_{[110]}$ and $k_{[1\bar{1}0]}$ as the orientation of the dominant slopes present on the surface are along the high-symmetry directions on the (001) surface. Lines of high intensity in such a diffractogram are oriented perpendicular to facets at the illuminated/shadow and the left/right sides of the mounds, respectively. We will refer to them as facet truncation rods. Figure 7 shows experimental and simulated results obtained after depositing 35 ML at $T=230$ K at a polar angle of incidence of 80° .

Both the perpendicular and parallel phases are represented by their normalized values: $k_{[110]}$ and $k_{[1\bar{1}0]}$ are expressed in % Brillouin zone (%BZ). 100%BZ corresponds to $2\pi/a$, where $a=2.55$ Å denotes the in-plane lattice constant. The perpendicular momentum $k_{[001]}$ is represented by the phase S_z relating to $k_{[001]}$ by $k_{[001]}=\sqrt{2}S_z(2\pi/a)$.

Indeed, at the illuminated side (positive $k_{[110]}$) in Fig. 7 two quite well-defined parallel facet truncation rods can be discerned at an angle of about 52° with the vertical axis. One of these starts from $(k, S_z)=(0\%, 4)$, while the other originates from $(k, S_z)=(100\%, 3.5)$. The presence of these parallel rods indicates that we do not have a large $\{111\}$ -vicinal-oriented facet, as this would lead to a single rod from

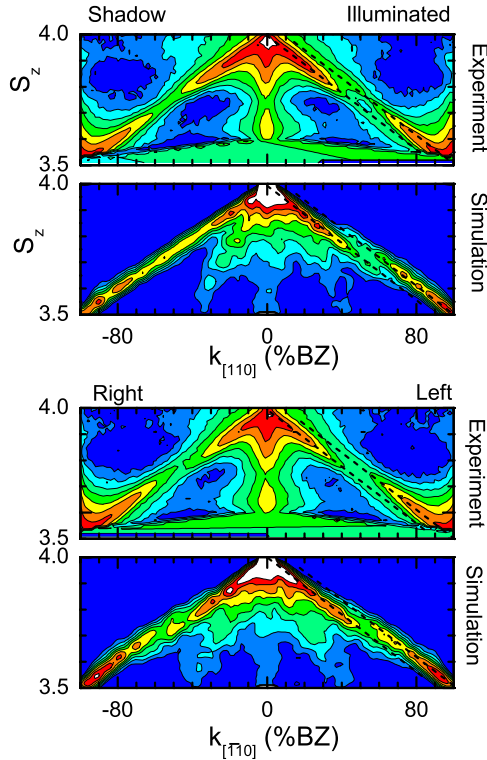


FIG. 7. (Color online) The diffracted intensity in $k_{[110]}-S_z$ (left) and $k_{[1\bar{1}0]}-S_z$ planes (right). The intensity rods represent the average slopes of the mound facets present at the illuminated and shadow side (top images) and left and right sides (bottom images). The top panels show experimental results, while the bottom ones display simulation results. The surface morphology is obtained after deposition of 35.4 ML at a polar angle of incidence of 80° at $T = 230$ K. The color scale used to indicate the intensity variation is similar to the one used in Fig. 6.

$(k, S_z) = (0\%, 4)$ to $(k, S_z) = (100\%, 3.5)$. The overall slope of the observed rods on the illuminated side is 52° , just below the 54.7° of a $\{111\}$ facet with respect to the $\{100\}$ base plane. This reduced angle and the appearance of two parallel rods reflect the limited width of these terraces, i.e., the slope contains at least two terraces with a $\{111\}$ orientation. The separation between the parallel facet truncation rods reflects the average width of these terraces.³⁰ The simulated and the experimentally observed separations ($\Delta k_{[110]} = 10\%$ BZ) at the illuminated side are identical within 0.5° , the accuracy of the results. At the shadow side a well-defined facet rod at 54.7° is observed. The diffraction plane on the left and the right sides show a very similar facet rod behavior as seen for the illuminated side.

Very similar results were found in experiments and simulations for 29 ML grown at 250 K. The illuminated side showed a slightly larger splitting in the two parallel facet rods of $\Delta k_{[110]} = 13\%$ BZ. In contrast to the situation at 230 K, the shadow side is not as clearly developed at 250 K and a combination of $\{111\}$ and $\{113\}$ microfacets is observed.

The influence of the deposition angle on the slopes of the mounds after a deposition of 40 ML at 250 K has already been extensively investigated experimentally.^{7,8} The result of these previous measurements and of the present simulations for similar conditions is shown in Fig. 8.

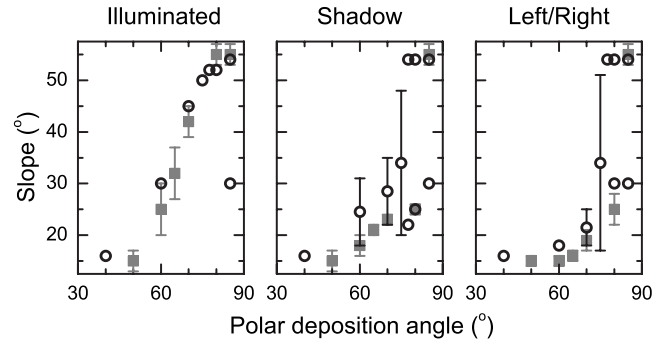


FIG. 8. Facet slopes after deposition of 40 ML as function of polar deposition angles. The gray squares refer to the experimental data points from van Dijken ($T = 250$ K, $R = 0.25$ ML/min) (Ref. 7). The black circles are results from the present simulations ($T = 250$ K, $R = 1$ ML/min).

Overall this figure shows very similar slopes of the mounds as a function of the deposition angle for the experimental and simulation results. Deposition angles ranging from normal incidence up to 50° result in the formation of $\{115\}$ facets at all sides. At larger off-normal incidence angles steeper slopes develop. Deposition at grazing incidence angles (above 75°) results in the steepest facets, representing $\{111\}$ facets, at all sides. In the range $60^\circ - 75^\circ$ the illuminated slopes develop into steeper slopes compared to the shadow side, while the left/right sides are still close to $\{115\}$ facets. For grazing incidence, the simulations indicate the presence of a combination of two facets at the shadow and left and right sides, a $\{111\}$ and a $\{113\}$ facet. The latter is less intense and therefore less clearly present. An analysis of the simulated morphologies shows that these $\{113\}$ facets are located at the bottom of the mound structures. The presence of these two facets is first noted for the shadow site. The development of these two facets for grazing incidence also leads to a rather large error bar in the results for less grazing incidence. They simply reflect the inability to discern between the two facets. Experimentally, the presence of two facets on one slope was only observed for extremely grazing incidence deposition (85°).²⁰

V. EVOLUTION OF SURFACE MORPHOLOGY IN FILMS GROWN AT GRAZING INCIDENCE

A. Formation of facets

The experimental observations are very similar to the results from an extensive, quantitative growth simulation. This similarity allows to study details and general aspects of the relation between the emergence of the elongated mounds as the result of the combined action of (temperature-dependent) adatom mobility, the deposition dynamics, and geometry. At grazing incidence the deposition dynamics is initially dominated by steering, while geometric shadowing becomes important in later stages. Both induce a strong heterogeneity in the deposition flux. The complex interplay between deposition dynamics and diffusion effects makes realistic simulations indispensable to understand the growth mode. This already starts in the submonolayer regime. The elongation of

the adatom islands perpendicular to the plane of incidence is a result of steering. An enhanced flux will impinge on top of an adatom island near the illuminated side. A large portion of this enhanced flux descends over the step edges of the adatom islands. This interlayer mass transport is similar for the four sides of a compact adatom island and will in the temperature regime considered take place almost exclusively via the kinks in the $\langle 110 \rangle$ step edges.¹⁴ However, the atoms that have landed on top of the adatom island are borrowed from the flux distribution in the direction of the deposition beam. This flux redistribution gives rise to a reduction in the island's growth rate parallel to the plane of incidence and the islands grow anisotropically.⁶⁻⁸ The elongation perpendicular to the deposition plane becomes more pronounced as more material is deposited giving an increased flux on the illuminated side of the elongated mounds.

Simulations around 2.5 ML show a slightly smaller number of kinks on the illuminated side of adatom islands. This decrease in the density of kinks has as a direct consequence that the interlayer mass transport decreases. The reduced interlayer transport initiates a faster nucleation in the next layer, which in turn increases the steering effect. In this way a cyclic pattern that accelerates roughening is created and with increased roughness, shadowing will start to influence the flux distribution. The accelerated roughening is faster at more grazing incidence and lower temperatures and leads to the formation of well-defined facets. The roughening itself is limited by the formation of the steepest possible facet, i.e. $\{111\}$ facets, facilitated by the fast adatom diffusion on these facets.

We attribute the presence of the two large terraces predominantly observed on the illuminated side of the mounds, to the particulars of the growth mode at oblique incidence deposition. Steering results in a relatively high flux at the top of the illuminated side. The newly deposited atoms diffuse rapidly over the upper $\{111\}$ terrace on the illuminated side and become incorporated in the step edge that separates the upper and the lower facet terraces. This step edge is a virtually impermeable barrier for diffusion to the lower terrace. A diffusion process over this step edge requires a local uphill diffusion step. The lower terrace expands while the upper terrace shrinks in size. The high flux on the illuminated side results in a very rapid movement of the $\langle 110 \rangle$ -step edge towards the top of the mound. Only when a step edge approaches the top of the mound, sufficient adatoms will be deposited on the lower terrace to facilitate the move of the next step edge up the side of the mound. This scenario explains the presence of, on average, only one step edge on the illuminated side in the simulated morphology. The illuminated facets grow in a local step propagation mode. This implies that the average length of the terrace as deduced from diffraction can be used as measure for the average height of the mounds in the plane of deposition. The average height can be calculated from the normalized separation along $k_{[110]}$ of the $\{111\}$ -like facet rods. After depositing 29 ML at a deposition angle of 80° at $T=250$ K, the separation of 13%BZ corresponds to a height $H=27.8$ ML (4.8 nm). The 10% difference observed for growth at 230 K results in a height of 36.1 ML (6.5 nm). These two values indicate a substantial stronger roughening of the growth front at the lower temperature.

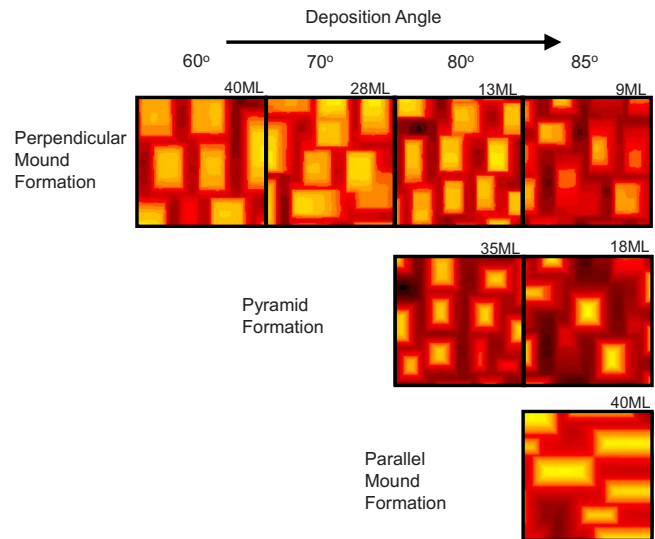


FIG. 9. (Color online) Two stages and their transition region in the evolution of growth at various oblique incidence angles at 250 K. Mound formation PER and PAR to the plane of incidence and the transition region characterised by the observation of pyramids.

The expansion rate of the illuminated side is limited by the shadow of the structure in front of it. This provides a mechanism that regulates the distance between mounds and leads to a highly regular pattern as observed in diffraction experiments for 10-ML-thick films. A very good ordering and a ripplelike pattern was found in simulations for a temperature of 270 K. The STM measurements do not show such a good ordering in the extended temperature range studied. This is probably due to shortcomings of the simulations. The activation barriers for interlayer mass transport may well alter on the very rough surfaces grown at oblique incidence deposition. Also, a slightly underestimated kink density can have a pronounced influence on the interlayer mass transport. In the experiments one also uses a deposition source with a finite angular spread, while the simulations use a zero angular spread.

B. Rotation of the mound elongation direction

Figure 9 shows the simulated morphology as a function of deposition angle and deposited amount at 250 K. Two different regions after the initial establishment of elongated mounds at very low coverages can be discerned in these images representing different stages in the growth: perpendicular (PER) and parallel (PAR) to the deposition plane. The rotation of the elongation direction from perpendicular to parallel to the deposition plane is characterized by a transition regime in which the surface is covered with pyramid-like structures. First the smallest mounds change their orientation, followed later by the larger ones. Diffraction experiments of growth in this stage⁸ yield a similar intensity and shape for all four facet peaks. These experiments showed a transition in intensity of the facets parallel and perpendicular to the plane of incidence. In the PER state the facet peaks in the deposition plane are substantially stronger, while these are the smaller ones in the PAR state. We estimate that this

TABLE I. Temperature dependence of the roughness determined under various conditions. The values from oblique incidence STM measurements are derived from the images shown in Fig. 2.

Method	T (K)	rms (Å)
STM	270	6.9 ± 0.6
STM	290	6.2 ± 0.6
STM	310	4.4 ± 0.2
Simulation	270	8.0
STM (Ref. 31)	300	4.0

scenario for the development of the mound shape is very generic in the kinetic growth regime, as it is observed for various deposition angles and temperatures. Also, for much higher interlayer transport barriers, this rotation was seen in simulations.¹³ The coverage at which the transition takes place increases with temperature and occurs at a later stage for less oblique incident deposition.

C. Enhanced roughening of the growth front

Surface roughness is a key parameter commonly employed to describe the average morphological properties of surfaces in general and of thin films in particular. The clear observation of terraces and individual step edges allow a straightforward height calibration of the STM images at elevated temperatures. The evaluated root mean square (rms) roughness in the temperature range 270–310 K is listed in Table I. For lower temperatures, the rms cannot be evaluated due to convolution of the atomic-scale morphology with the finite-size STM tip.

The increase in surface roughness with decreasing temperature is straightforwardly explained by a reduction in the interlayer mass transport. This is due to a finite Ehrlich-Schwoebel barrier. The value of the rms roughness at 310 K is very similar to the one reported for normal incidence growth at room temperature (4.0 Å).³¹ This similarity is expected given the absence of a visible anisotropy for grazing incidence deposition at 310 K, see Fig. 2. The kMC simulations at 270 K show a roughness of 8.0 Å. This is in reasonable agreement with the experimental value, albeit a stronger anisotropy is observed in the simulations. The terrace width determined from LEED measurements at 230 and 250 K and the simulation results of Fig. 7 show a much rougher growth front for these lower temperatures.

The simulations provide the opportunity for a detailed analysis of the evolution of the roughness with coverage. Scaling theory is often used to provide a theoretical context for the behavior of the interface roughness w .³² Kinetic roughening during multilayer growth develops according to this theory as $w \propto \theta^\beta$, where β is the kinetic roughening or growth exponent. Simulation results show that $\beta=0.5$ for growth at normal incidence and temperatures between 250 and 275 K.¹⁴ Below and above these temperatures lower values for β were found, indicating smoother growth in both cases. Figure 10 shows the roughness development for growth at a polar deposition angle of 40°.

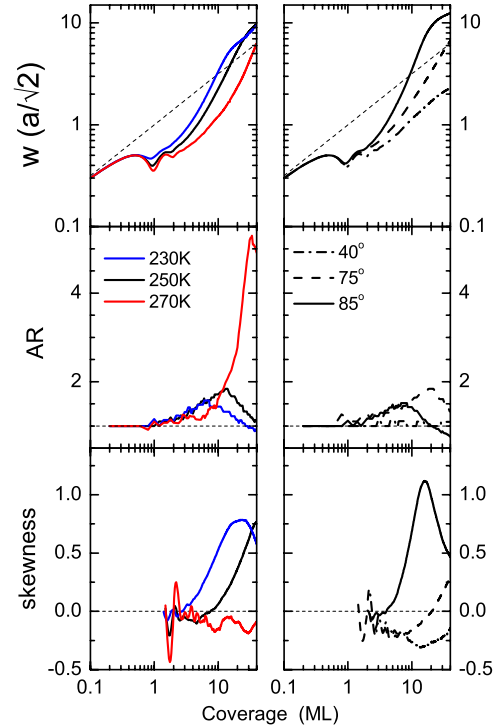


FIG. 10. (Color online) Top left: roughness development for 230, 250, and 270 K during growth at a deposition angle of 80°. Top right: roughness development for a deposition angle of 40°, 70°, and 85° at a temperature of 250 K. The deposition rate is 1 ML/min. The straight short dash line indicates the roughness development corresponding to Poisson growth, i.e., $\beta=0.5$. Middle panel: shape anisotropy AR as a function of coverage for various temperatures and deposition angles. Bottom: skewness as a function of coverage for various temperatures and deposition angles.

This roughness development is very similar to that for normal incidence growth. Initially a layer-by-layer growth is observed, followed by a regime characterized by an increase in roughness with coverage described by $\beta \approx 0.5$. An increase with such an exponent is depicted by the straight line. This value of the growth exponent is very often associated with a Poisson growth mode. The actual definition of the Poisson growth mode involves the deposition process on a simple cubic Kossel crystal with on-top adsorption sites and without any interlayer transport and avoiding vacancies. This is usually considered as the roughest solid-on-solid growth mode possible.³³ Grazing incidence deposition also shows at first a layer-by-layer-like evolution of the interface roughness, see Fig. 10. However, already after 3 ML the roughness starts to increase dramatically compared to normal incidence growth. In this regime, the growth cannot be characterized by a single exponent. A local value of β is defined as

$$\beta(\theta) = \frac{dw/w}{d\theta/\theta} \quad (1)$$

with θ the amount of material deposited. The local-growth exponent becomes significantly larger than the Poisson value of $\beta=0.5$ indicated by the straight line in Fig. 10. For very grazing incidence (85°), we find a value of $\beta=1.8$ around 10

ML coverage and this growth behavior is therefore denoted as “super Poisson” roughening. Note that also in this case, layer-by-layer growth is observed initially. Under these conditions, not only the local exponent is very large but also the value of the roughness itself becomes substantially larger than the value that would be obtained for continuous Poisson growth.

The influence of substrate temperature on the roughness is illustrated for a grazing deposition angle of 80° in Fig. 10. The coverage at which the roughness enhancement starts decreases with temperature.

D. Evolution of the mound shape

The lateral mound shape is characterized by the aspect ratio. The AR was derived from the central peak in the autocorrelation image of the surface morphology in a similar manner as for the STM images. The change in increase in the roughness, i.e., a decrease in β is accompanied by the change in orientation of the elongation direction, see Fig. 10. The highest aspect ratio is found to coincide with the maximum value of β . The situation $AR=1$, at which the morphology is dominated by pyramids (i.e., the region previously denoted with “transition regime”), shows already a significant decrease in β . This is best observed for the situations at 230 and 250 K for grazing incidence deposition. At 270 K and for a deposition angle of 75° , this is less obvious as the elongation rotation is expected to take place at coverages beyond 40 ML.

The evolution of the average mound shape perpendicular to the interface can be quantified with the moments of the height distribution. The first moment provides the average height, the second moment the interface width w , while the third moment or skewness provides direct insight in the asymmetry of the height distribution.³⁴ The skewness is also displayed in Fig. 10. The extremum in the skewness lies just before the transition in the elongation direction, $AR=1$. The surface starts to be covered with pyramidlike structures. The large positive value of the skewness indicates a quite asymmetric height distribution, with many more exposed layers in the top side of the mound, indicative of a substantial uphill current. This asymmetry is initially found in the opposite direction for the higher temperatures and lower deposition angles. The absence of negative skewness values for 230 K and for very grazing incidence is due to the very strong roughening that already takes place for low coverages.

The transition towards columnar growth as observed in many heteroepitaxy experiments is probably suppressed due to the low barrier for diffusion on the $\{111\}$ facets. Columnar growth is expected only if nucleation of islands can take place on sufficiently large facets.

Our final approach to provide quantitative insight in the exposed layer distribution is the so-called wedding cake model, which was introduced to describe the average shape of mounds observed in homoepitaxial growth of Pt(111).^{33,35,36} In this model the average surface area of a layer in the mound is represented by the radius of a disk with the same area. A plot of the layer height versus the disk radius reflects the average side view of the mounds, i.e., the

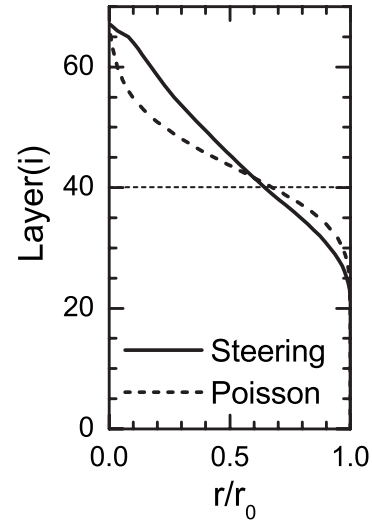


FIG. 11. The average radius r_i of layer A_i for grazing incidence growth (solid line) and Poisson growth (dashed line) is depicted. The average radius of the layer is normalized to the average radius of the mounds r_0 .

cake profile. For Pt(111) a fair similarity in shape between the actually grown mounds and Poisson distributed growth was observed. The layer distribution of the anisotropic mounds can also be analyzed by this wedding cake model. However, the anisotropy itself is first removed by transforming the layer coverage into circular discs. For grazing incidence growth at 230 K, a mound shape analysis is depicted in Fig. 11 for a 40-ML-thick Cu film on Cu(001). A much broader distribution is observed for grazing incidence growth compared to a Poisson distribution. The average shape after grazing incidence growth consists of several straight sections, illustrating extensive facet formation. The steepest slope is found just below the top of the mounds. Compared to Poisson growth, a smaller amount of material is present at the larger radii. This mass has been transferred to islands with a small radius, located at higher layer levels than in Poisson growth. Such a phenomenon (super Poisson roughening) requires a so-called uphill flux. The required extensive uphill flux is a true signature of a considerably heterogeneous flux distribution, i.e., flux steering to the highest protrusions. The top layer in grazing incidence growth has a relatively small area.

VI. SUMMARY AND CONCLUSION

A great similarity between growth simulations and STM and diffraction experiments in terms of the rotation of the elongation direction of the mounds, a strong roughening and the formation of facets with a specific orientation and a limited terrace width was found. This similarity allows us to use the simulation scheme to analyze growth at oblique incidence in great detail. The established accuracy of the simulation scheme used is the result of an accurate incorporation of both interlayer transport and the steering effect. Of special interest for oblique incidence growth is the illuminated side of the mounds. These are formed after deposition of only a

few layers and a strong increase in slope was found, while the shadow side and left and right hand sides show this strong increase much later. This culminates in the development of {111} facets first at the illuminated side, followed later by the other three sides. This growth behavior is observed for the temperatures studied in the simulation, i.e., 230–270 K and for polar angles of incidence above 70°.

Both experiment and simulation show that extreme roughening occurs at grazing incidence deposition. The rms roughnesses evaluated from the simulated morphology support this observation and show a roughening behavior with a growth exponent β much larger than the Poisson value of 0.5. Oblique incidence deposition thus leads to super Poisson roughening. The extreme roughening coincides with a change in elongation direction of the mounds, which occurs via the formation of square-pyramid structures. At this stage, also a very broad and skewed distribution of the height distribution is observed. After rotation, large elongated islands parallel to the deposition beam are formed. However, the ordering of the structures remains the same, i.e., a well-defined distance in the direction parallel to the deposition beam is conserved.

Discrepancies between the simulated and experimentally observed morphology are a higher mound density and a larger aspect ratio of the mounds in the simulations. A possible candidate responsible for the observed discrepancies is

the angular spread in the atomic beam, which is much larger in our experiments than in the simulation. Moreover, the oversimplified surface diffusion of the simulations may contribute as well: stress and strain effects are not implemented in the simulations. For heteroepitaxially grown films, the strain has a drastic influence on the surface diffusion and nucleation processes and thus on the final surface morphology.³⁷ Although for homoepitaxial growth the classical theory assumes no mismatch between the substrate and the deposited film, theoretical calculations predict a slight strain present in monoatomic height islands.³⁸ Especially for small structures, we expect large strain fields which could lead to significant changes in diffusion barriers. The good correspondence between the experimental and simulation results observed in the presented data provide a solid foundation for the study the influence of the steering effect in the evolution of the morphology during growth.

ACKNOWLEDGMENTS

This work is part of the research programme of the Stichting Fundamenteel Onderzoek der Materie (FOM), financially supported by the Nederlandse Organisatie voor Wetenschappelijk Onderzoek (NWO).

*h.wormeester@utwente.nl

- ¹J. M. Nieuwenhuizen and H. B. Haanstra, *Philips Tech. Rev.* **27**, 87 (1966).
- ²L. Abelmann and C. Lodder, *Thin Solid Films* **305**, 1 (1997).
- ³G. Beydaghyan, K. Kaminska, T. Brown, and K. Robbie, *Appl. Opt.* **43**, 5343 (2004).
- ⁴H. E. Ruda *et al.*, *Nanoscale Res. Lett.* **1**, 99 (2006).
- ⁵S. L. Zeder, J. F. Silvain, M. E. Re, M. H. Kryder, and C. L. Bauer, *J. Appl. Phys.* **61**, 3804 (1987).
- ⁶H. Wormeester and B. Poelsema, *Phys. Rev. B* **66**, 165406 (2002).
- ⁷S. van Dijken, L. C. Jorritsma, and B. Poelsema, *Phys. Rev. Lett.* **82**, 4038 (1999).
- ⁸S. van Dijken, L. C. Jorritsma, and B. Poelsema, *Phys. Rev. B* **61**, 14047 (2000).
- ⁹S. van Dijken, G. Di Santo, and B. Poelsema, *Appl. Phys. Lett.* **77**, 2030 (2000).
- ¹⁰S. van Dijken, G. Di Santo, and B. Poelsema, *Phys. Rev. B* **63**, 104431 (2001).
- ¹¹N. Shevchik, *J. Non-Cryst. Solids* **12**, 141 (1973).
- ¹²L. C. Jorritsma, Ph.D. thesis, University of Twente, 1997.
- ¹³Y. Shim and J. G. Amar, *Phys. Rev. Lett.* **98**, 046103 (2007).
- ¹⁴F. L. W. Rabbering, H. Wormeester, F. Everts, and B. Poelsema, *Phys. Rev. B* **79**, 075402 (2009).
- ¹⁵H.-J. Ernst, F. Fabre, and J. Lapujoulade, *Surf. Sci.* **275**, L682 (1992).
- ¹⁶H.-J. Ernst, F. Fabre, R. Folkerts, and J. Lapujoulade, *J. Vac. Sci. Technol. A* **12**, 1809 (1994).
- ¹⁷H.-J. Ernst, F. Fabre, R. Folkerts, and J. Lapujoulade, *Phys. Rev. Lett.* **72**, 112 (1994).
- ¹⁸F. L. W. Rabbering, Ph.D. thesis, University of Twente, 2008.
- ¹⁹F. L. W. Rabbering, A. Kara, H. Wormeester, T. Warnaar, O. Trushin, T. S. Rahman, and B. Poelsema, *Phys. Rev. Lett.* **103**, 096105 (2009).
- ²⁰S. van Dijken, Ph.D. thesis, University of Twente, 2000.
- ²¹U. Linke and B. Poelsema, *J. Phys. E* **18**, 26 (1985).
- ²²L. C. Jorritsma, M. Bijmagne, G. Rosenfeld, and B. Poelsema, *Phys. Rev. Lett.* **78**, 911 (1997).
- ²³B. Poelsema, L. K. Verheij, and G. Comsa, *Phys. Rev. Lett.* **51**, 2410 (1983).
- ²⁴L. K. Verheij, B. Poelsema, and G. Comsa, *Surf. Sci.* **162**, 858 (1985).
- ²⁵B. Poelsema, A. F. Becker, G. Rosenfeld, R. Kunkel, N. Nagel, L. K. Verheij, and G. Comsa, *Surf. Sci.* **272**, 269 (1992).
- ²⁶P. Bedrossian, G. Poelsema, B. Rosenfeld, L. C. Jorritsma, N. N. Lipkin, and G. Comsa, *Surf. Sci.* **334**, 1 (1995).
- ²⁷O. Biham, I. Furman, M. Karimi, G. Vidali, R. Kennett, and H. Zeng, *Surf. Sci.* **400**, 29 (1998).
- ²⁸J. W. Evans, *Phys. Rev. B* **43**, 3897 (1991).
- ²⁹A. Bogicevic, S. Ovesson, P. Hyldgaard, B. I. Lundqvist, H. Brune, and D. R. Jennison, *Phys. Rev. Lett.* **85**, 1910 (2000).
- ³⁰G. Comsa, G. Mechttersheimer, B. Poelsema, and S. Tomoda, *Surf. Sci.* **89**, 123 (1979).
- ³¹J. K. Zuo and J. F. Wendelken, *Phys. Rev. Lett.* **78**, 2791 (1997).
- ³²A. L. Barabási and H. E. Stanley, *Fractal Concepts in Surface Growth* (Cambridge University Press, Cambridge, 1995).
- ³³T. Michely and J. Krug, *Islands, Mounds and Atoms* (Springer, New York, 2004).
- ³⁴Y. Zhao, G.-C. Wang, and T.-M. Lu, *Characterization of Amorphous and Crystalline Rough Surface: Principles and Applica-*

- tions*, Experimental Methods in Physical Sciences Vol. 37 (Academic, New York, 2001).
- ³⁵J. Krug, J. Stat. Phys. **87**, 505 (1997).
- ³⁶M. Kalf, P. Smilauer, G. Comsa, and T. Michely, Surf. Sci. **426**, L447 (1999).
- ³⁷H. Brune, K. Bromann, H. Röder, K. Kern, J. Jacobsen, P. Stoltze, K. Jacobsen, and J. Norskov, Phys. Rev. B **52**, R14380 (1995).
- ³⁸O. V. Lysenko, V. S. Stepanyuk, W. Hergert, and J. Kirschner, Phys. Rev. Lett. **89**, 126102 (2002).